Fully relativistic first-principles quantum transport simulation of noncollinear spin transfer and spin Hall current

Zhiyi Chen,[1,2,3] Qingyun Zhang,[1] Zhe Yuan,[4] Jianpeng Liu,[1] Ke Xia,[5] and Youqi Ke[1,2,3,*]

[1]*School of Physical Science and Technology, ShanghaiTech University, Shanghai 201210, China*
[2]*Shanghai Institute of Optics and Fine Mechanics, Chinese Academy of Sciences, Shanghai 201800, China*
[3]*University of Chinese Academy of Sciences, Beijing 100049, China*
[4]*Department of Physics, Beijing Normal University, Beijing 100875, China*
[5]*Department of Physics, Southeast University, Nanjing 100193, China*

(Received 31 December 2022; accepted 24 April 2023; published 24 May 2023)

In this work, we report the fully relativistic (FR) first-principles quantum transport simulation of noncollinear spin transfer and spin Hall current in the device structure. In this method, the noncollinear FR exact muffin-tin orbital method is combined with Keldysh's nonequilibrium Green's function approach and mean-field theory to account for the multiple disorder scattering. We adopt the Bargmann-Wigner polarization operator to define the appropriate FR spin current so that the current-induced spin transfer, in the noncollinear magnetic device or due to the spin Hall effect, can be studied from first principles. As applications, we calculate the spin transfer torque in noncollinear spin valves Co/Cu/FM/Cu (FM = Co, $Ni_{0.8}Fe_{0.2}$) and spin Hall angles in various $Pt_{1-x}Y_x$ [Y = vacancy (Va), Au, Ag, Pd] alloys. We find that our FR results agree well with previous theoretical simulations and experimental measurements. Moreover, it is found that the applied finite bias can significantly enhance the spin Hall angle in $Pt_{1-x}Va_x$, and PtAg alloy presents a much higher spin Hall angle than that of PtAu and PtPd alloys. Our implementation of the FR method provides an important first-principles tool for studying various nonequilibrium spin phenomena and the associated relativistic effects in realistic device structures with atomic disorders, including both current-induced spin transfer and spin-orbit torques.

DOI: 10.1103/PhysRevB.107.195431

I. INTRODUCTION

Spin transport plays the central role in the field of spintronics, possessing important applications in magnetic memories, oscillators, and spin logics [1–3]. Presently, current-induced spin torque has provided a fundamental approach for realizing the efficient electrical manipulation of magnetism, and it has attracted enormous research attention in science and technologies for important applications in spintronic devices [4]. For example, spin transfer torque (STT) carried by spin-polarized current, as first introduced by Slonczewski [5] and Berger [6], can effectively switch the magnetic orientation in spin valve devices, providing the main stream for controlling the bit states in STT-based magnetic random-access memory. Moreover, as a complement to STT, current-induced spin-orbit torques (SOT) have been successfully utilized to manipulate the magnetic order, domain walls, and skyrmions, opening novel designs for spintronic applications [4,7]. For spin-orbit torque, two main mechanisms have been proposed, including the spin Hall effect [8–11] and the inverse spin galvanic effect [12–16], as the nonequilibrium phenomena of the relativistic effect. The materials system for studying current-induced spin transport has extended from simple magnetic multilayers to those containing heavy metals, topological insulators, etc., from ferromagnetic to antiferromagnetic systems, and from collinear to noncollinear magnetic materials. The theoretical simulation of STT and SOT calls for the full quantum treatment for the dependence on material and interface electronic structures. At present, the simulations based on the first-principles method have played very important roles in understanding the current-induced spin transport phenomena and identifying new effects, e.g., the fully first-principles simulation of STT in magnetic multilayers [17], the demonstration of the important interface-enhanced spin Hall angle [18], and the interface-generated spin current [19]. It has been theoretically predicted that noncollinear antiferromagnetic materials can present spin polarization current, presenting promising applications in spintronic devices [20,21]. Moreover, it has been known that the presence of disorder scattering is crucial for the generation of the spin Hall effect [22,23]. Therefore, it is now clear that an effective simulation method to calculate current-induced spin transport with general applicability acquires the capabilities to (i) effectively handle the noncollinear magnetism, which is quite ubiquitous in magnetic materials; (ii) account for the relativistic effects [e.g., spin-orbit interaction (SOI) mediating the transfer of angular momentum between the orbital and spin]; (iii) effectively treat the influence of inevitable random imperfections including chemical, lattice, and magnetic disorders; and (iv) sophisticatedly handle the nonequilibrium condition with current flow in the operating devices, presenting important challenges for the presently available first-principles simulations.

In previous works, we developed the first-principles quantum transport method in the framework of the exact muffin-tin orbital (EMTO) -based density functional theory

*keyq@shanghaitech.edu.cn

(DFT) [including both scalar and full relativistic (SR/FR)], combined with the nonequilibrium Green's function technique (NEGF) for collinear magnetic systems [24,25], and we realized first-principles nonequilibrium mean-field theory [including the nonequilibrium dynamical cluster approximation (DCA) [26–29] and the coherent potential approximation (CPA) [30,31] combined with nonequilibrium vertex correction [32–34]] for effectively treating the disorder scattering in quantum transport [28]. The EMTO method features the highly localized and minimal basis, and at the same time allows the large overlapping muffin-tin potential spheres to treat both the interstitial and atomic regions on the same footing [35–40], beyond the second-generation MTO and providing a suitable approach for first-principles quantum transport simulations [41]. With these important bases, the main goal of this work is to report the implementation of a fully relativistic quantum transport method for calculating the noncollinear spin transfer and spin Hall current from first principles, as an important extension of the EMTO-DFT-NEGF method. We formulate the nonequilibrium density matrix for noncollinear magnetic devices in the framework of the fully relativistic EMTO, and we utilize the Bargmann-Wigner polarization operator $\hat{T}_\mu = (\hat{T}, \hat{T}_4)$ [42] for the fully relativistic spin current formula. Such a NEGF-based fully relativistic spin transport formalism enables the simulation of spin current in real device structure under nonequilibrium conditions, beyond the linear-response calculations. We also provide a detailed investigation of the spin current in the nonrelativistic limit, which contains conventional spin-current terms and other terms in the order of $1/c^2$ that may effectively contribute to the spin Hall current due to the relativistic effects. As applications, we calculate the spin transfer in spin valves Co/Cu/FM/Co (FM = Co, $Ni_{0.8}Fe_{0.2}$) and the spin current due to spin Hall effects in various disordered $Pt_{1-x}Y_x$(Y = vacancy, Au, Pd, Ag) alloys, and the comparison with other theoretical methods and experimental measurements is discussed.

The rest of the paper is organized as follows: Section II introduces the fully relativistic noncollinear EMTO method and Keldysh's NEGF representation for transport simulation of a device structure (with disorder). Section III introduces an appropriate fully relativistic spin current formula and its average over disorders inevitable in realistic devices. In Sec. IV, we present some information about the implementation and numerical results and discussions. Finally, we conclude our work in Sec. V with a detailed derivation of spin current in the nonrelativistic limit, and we present associated discussions in Appendix A.

II. FULLY RELATIVISTIC EXACT MUFFIN-TIN ORBITAL METHOD FOR A NONCOLLINEAR MAGNETIC DEVICE

We consider the general Kohn-Sham Dirac Hamiltonian for a noncollinear magnetic device system as shown in Fig. 1, for which we are interested in the spin transport properties,

$$\hat{H} = c\vec{\alpha}\cdot\vec{p} + (\beta - I_4)mc^2 + V(\vec{r}) + \beta\vec{\Sigma}\cdot\vec{B}(\vec{r}) \tag{1}$$

and

$$\vec{\alpha} = \begin{pmatrix} 0 & \vec{\sigma} \\ \vec{\sigma} & 0 \end{pmatrix}, \quad \beta = \begin{pmatrix} I_2 & 0 \\ 0 & -I_2 \end{pmatrix}, \quad \vec{\Sigma} = \begin{pmatrix} \vec{\sigma} & 0 \\ 0 & \vec{\sigma} \end{pmatrix}, \tag{2}$$

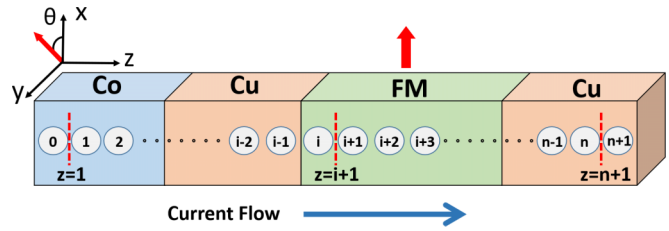

FIG. 1. Schematic illustration of a two-probe device with noncollinear spin: Co/Cu/FM/Cu magnetic multilayers. In our calculations, the magnetization of FM is fixed and that of Co is variable. θ is the relative angle between the magnetization of Co and FM. The layer $1 \leqslant z \leqslant n$ is for the central device; $z \leqslant 0$ and $z \geqslant n+1$ are for the left and right electrodes, respectively.

where σ is the Pauli matrix. In the muffin-tin approximation, the effective full potential $V(\vec{r})$ is approximated as

$$V(\vec{r}) \approx V_{\rm mt}(\vec{r}) \equiv V_{\rm mtz} + \sum_R [V_R(r_R) - V_{\rm mtz}], \tag{3}$$

where $V_{\rm mtz}$ is the muffin-tin zero, and $V_R(r_R)$ is a spherical potential centered on lattice site R (the notation $\vec{r}_R = \vec{r} - \vec{R}$ and $r_R = |\vec{r}_R|$). It should be mentioned that EMTO allows the large overlapping potential spheres to reduce the error. The field $\vec{B}_{\rm mt}(\vec{r})$, which describes the exchange splitting, can be written (in the muffin-tin approximation) as

$$\vec{B}(\vec{r}) \approx \vec{B}_{\rm mt}(\vec{r}) \equiv \sum_R B_R(r_R)\vec{n}_R, \tag{4}$$

where $\vec{n}_R$ denotes the magnetic field direction, and it can be different for each site, namely the noncollinear magnetization.

The Kohn-Sham Dirac equation, namely $H\Psi = E\Psi$, for a general magnetic system can be solved efficiently by introducing the four-component FR-EMTO [35–40], namely

$$\Phi^{a,G}_{R\Lambda}(\epsilon, \vec{r}_R) = \phi^{a,G}_{R\Lambda} - \varphi^{a,G}_{R\Lambda} + \psi^{a,G}_{R\Lambda}, \tag{5}$$

where $\phi^{a,G}_{R\Lambda}$, $\varphi^{a,G}_{R\Lambda}$, and $\psi^{a,G}_{R\Lambda}$ are the respective partial wave, the free-electron solution, and the screened spherical wave (SSW), and the relativistic quantum number is $\Lambda = \kappa\mu$. Here, the superscript a denotes the screening representation, G denotes the quantity defined in the global coordinate framework (as shown in Fig. 1, $\vec{e}^G_z$ is the transport direction in which the device is not periodic), $\phi^{a,G}_{R\Lambda}$ and $\varphi^{a,G}_{R\Lambda}$ are defined within the potential sphere, and $\psi^{aG}_{R\Lambda}$ is highly localized in the interstitial region. In the global framework, only the SSW can be straightforwardly obtained as

$$\psi^{a,G}_{R\Lambda}(\kappa^2, \vec{r}_R) = f^{a,G}_{R\Lambda}(\kappa^2, \vec{r}_R)\delta_{RR'} - \sum_{R'\Lambda'} g^{a,G}_{R'\Lambda'}(\kappa^2, \vec{r}_{R'}) S^{aG}_{R'\Lambda',R\Lambda}(\kappa^2), \tag{6}$$

which is obtained as the solution for $[c\vec{\alpha}\cdot\vec{p} + (\beta - I_4)mc^2 - \kappa^2]\psi^{aG}_{R\Lambda}(\kappa^2, \vec{r}_R) = 0$ by enforcing the screening conditions [35,36,40] ($\kappa^2 = E - V_{\rm mtz}$), and f^a and g^a are the linear combination of the Bessel and Neumman functions (the same as the nonmagnetic case) [25]. Here, S^{aG} is the screened slope matrix and is highly sparse. However, to obtain the $\phi^{aG}_{R\Lambda}$ and $\varphi^{aG}_{R\Lambda}$ for the FR-EMTO in Eq. (5), we can first define the $\phi^{aL}_{R\Lambda}$, $\varphi^{aL}_{R\Lambda}$ inside each potential sphere in the local coordinate

framework of site R set by $\vec{n}_R$ as the local $\vec{e}_z^L$ axis. As a result, for a spin-polarized sphere, we have for the partial wave

$$\phi_{R\Lambda}^{a,L}(E,\vec{r}_R) = \sum_{\lambda=\kappa,-\kappa-1} \phi_{R\lambda\mu}^{a,L} N_{R,\lambda\kappa}^{aL,\mu}, \tag{7}$$

and for the free-electron solution

$$\varphi_{R\Lambda}^{a,L} = f_{R\Lambda}^{a,L} - \sum_{\lambda=\kappa,-\kappa-1} g_{R\lambda\mu}^{a,L} D_{R,\lambda\kappa}^{aL,\mu}, \tag{8}$$

where $[c\vec{\alpha}\cdot\vec{p} + (\beta - I_4)mc^2 + V_R(r_R) + \beta\Sigma_{\vec{n}_R}\cdot B_R(r_R)]\phi_R^L = E\phi_R^L$, and the N and D functions are determined from the matching condition at the potential sphere boundary [40] (for more information about the solution of $\phi_R^{a,L}$ and $\varphi^{a,L}$, refer to Refs. [40,41]).

Then, $\phi^{a,G}$ and $\varphi^{a,G}$ are connected to $\phi^{a,L}$ and $\varphi^{a,L}$ by the relation

$$\phi_R^{a,G} = \phi_R^L U_R(\alpha_R,\beta_R,\gamma_R) \tag{9}$$

and

$$\varphi_R^{a,G} = \varphi_R^L U_R(\alpha_R,\beta_R,\gamma_R), \tag{10}$$

where the unitary rotational matrix U_R is for the spin-spherical-harmonics part and describes the rotation from the local (at site R) to global coordinate frameworks by the Euler angle $(\alpha_R,\beta_R,\gamma_R)$ [43]. As an important result, one can find the overlap and Hamiltonian matrix elements of FR-EMTO for the noncollinear system in the global framework [25,44], namely

$$O^G = \langle\Phi^{a,G}|\Phi^{a,G}\rangle = a\dot{S}^{aG} - a\dot{D}^{aG}, \tag{11}$$

$$\langle\Phi^{a,G}|\epsilon - \hat{H}|\Phi^{a,G}\rangle = aS^{aG} - aD^{aG}, \tag{12}$$

where $D_R^{aG} = U_R^\dagger D_R^{a,L} U_R$ in which the on-site matrix D_R^{aL} is calculated in the local framework of R. Here, D^{aG} is a site-diagonal quantity determined by the atomic species, and S^{aG} describes the geometric structure of materials.

To implement the noncollinear FR-EMTO formalism for first-principles simulation of electron and spin transport, we introduce the contour-ordered Green's function (GF) in Keldysh's 2×2 matrix representation (in bold) [45,46], namely $\boldsymbol{G} = \begin{pmatrix} G^{\mathcal{A}} & 0 \\ G^{\mathcal{K}} & G^{\mathcal{R}} \end{pmatrix}$, where $G^{\mathcal{R}/\mathcal{A}/\mathcal{K}}$ are the respective retarded, advanced, and Keldysh's GFs, with which all other real-time GFs on the closed time contour can be obtained as their linear combinations [34], e.g., the lesser GF $G^< = \frac{1}{2}(G^K + G^A - G^R)$. Keldysh's NEGF technique has provide a powerful tool for treating a complex physical system at nonequilibrium condition. For a representative device structure shown in Fig. 1, for the central device region with an open boundary, $\boldsymbol{G}_{CC}^{aG} = \{a_C[\boldsymbol{S}_{CC}^{aG} - \boldsymbol{D}_C^{aG}] - \boldsymbol{\Sigma}_{ld}^{aG}\}^{-1}$ in which we use Keldysh's representation for the quantities $\boldsymbol{D}_C^{aG} = \begin{pmatrix} D_C^{aG,\mathcal{A}} & 0 \\ 0 & D_C^{a,\mathcal{R}} \end{pmatrix}$, $\boldsymbol{S}_R^{aG} = \begin{pmatrix} S_C^{aG,\mathcal{A}} & 0 \\ 0 & S_C^{aG,\mathcal{R}} \end{pmatrix}$, and $\boldsymbol{\Sigma}_R^{aG} = \begin{pmatrix} \Sigma_{ld}^{aG,\mathcal{A}} & 0 \\ \Sigma_{ld}^{aG,\mathcal{K}} & \Sigma_{ld}^{aG,\mathcal{R}} \end{pmatrix}$ for the self-energy due to electrodes. Here we consider the realistic device region containing disorders, denoted by the A_xB_{1-x} alloy model, for which, in the present FR-EMTO, only the site-diagonal $\boldsymbol{D}_{C,R}^{aG}$ is a random quantity depending on the random occupants A or B. Disorders can present an important influence on the device properties by changing the transport to diffusive regime. For such a disordered device, we have implemented the self-consistent nonequilibrium mean-field theory to calculate the averaged GFs, namely [24,25,28,34]

$$\overline{\boldsymbol{G}_{CC}^{aG}} = \left\{a_C\left[\boldsymbol{S}_{CC}^{aG} - \boldsymbol{\mathcal{D}}_C^{aG}\right] - \boldsymbol{\Sigma}_{ld}^{aG}\right\}^{-1}, \tag{13}$$

where $\mathcal{D}_R^{aG}$ describes the effective medium for the disorder-averaged central device, containing the important nonequilibrium statistics and multiple disorder scatterings. By calculating the averaged $\overline{\mathbf{G}_{CC}^{aG}}$, we can obtain the averaged quantum transport properties, including the electron transmission and spin current (for more information, please refer to Refs. [25,28]).

III. FULLY RELATIVISTIC SPIN CURRENT

For the spin current calculation, it has been discussed that the central issue is to define an appropriate spin current operator in the presence of a relativistic interaction, e.g., SOI, due to the nonconservation of spin [47,48]. For the spin operator, it is known that the use of $\frac{1}{2}\beta\vec{\Sigma}$ and $\frac{1}{2}\vec{\Sigma}$ present a negligible difference in the DFT calculation of the spin density and the magnetic moment, due to the tiny contribution of a small component χ in $\Psi = \binom{\psi}{\chi}$ satisfying $\hat{H}\Psi = E\Psi$ in material systems [41]. Based on the continuity equation for the spin density, it is thus natural that one can obtain the two definitions of spin current tensor, namely $J_i^{S_j,1} = \frac{1}{2}\Psi^\dagger c\alpha_i\Sigma_j\Psi$ and $J_i^{S_j,2} = \frac{1}{2}\Psi^\dagger c\alpha_i\beta\Sigma_j\Psi$, where $c\vec{\alpha}$ is the velocity operator. However, we can find that both definitions are problematic for general indexes i and j. For example, one can show that $J_i^{S_j,1\dagger} = -J_i^{S_j,1}$ for $i \neq j$ and $J_i^{S_i,2\dagger} = -J_i^{S_i,2}$ for $i = j$, demonstrating the fact that both $\vec{J}^{S,1}$ and $\vec{J}^{S,2}$ are not general (which may even present unphysical terms in the nonrelativistic limit). To avoid these problems in spin current in this work, we adopt the Bargmann-Wigner spin polarization operator $\hat{T}_\mu = (\hat{T},\hat{T}_4)$ [42] which was first used to define the spin current density tensor in Ref. [49] (later used in Refs. [50–52] to calculate the anomalous and spin Hall effects in the linear-response theory with the first-principles KKR method), namely

$$\begin{aligned} J_i^{S_j} &= \Psi^\dagger(c\alpha_i\hat{T}_j)\Psi \\ &= \Psi^\dagger\left(c\alpha_i\beta\Sigma_j + \frac{\Sigma_i\hat{p}_j}{m}\right)\Psi, \end{aligned} \tag{14}$$

which can present physical results for all the combinations of i and j. It should be mentioned that T_μ commutes with the field-free Dirac Hamiltonian presenting a conserved T_μ in vacuum, while the spin operators $\frac{1}{2}\beta\vec{\Sigma}$ and $\frac{1}{2}\vec{\Sigma}$ do not. As we show in Appendix A, for the nonrelativistic limit of the $J_i^{s_j}$ of Eq. (3), the zeroth-order term (in $\frac{1}{c^2}$) $J_x^{S_j,(0)} = \frac{i\hbar}{2m}\psi^\dagger[\sigma_j(\overleftarrow{\nabla} - \overrightarrow{\nabla})_x]\psi + \frac{\hbar}{2m}\phi^\dagger\{\sigma_j[(\overleftarrow{\nabla} + \overrightarrow{\nabla})\times\vec{\sigma}]_x\}\phi$, which contains the conventional spin current in the first term and the moving-dipole induced bound current contribution in the second. It can be shown that the divergence of the moving-dipole term presents zero divergence, presenting no contribution to the spin torque as expected (see Appendix A). Here, as we show in Appendix A, it should be mentioned that adding $\frac{\Sigma_i\hat{p}_j}{m}$ to

$c\alpha_i\beta\Sigma_j$ in Eq. (14) is critical for the physically correct $J_i^{S_j,(0)}$, making Eq. (14) general for the spin current tensor (especially for the case $i = j$). Moreover, the first order of the spin current in $1/c^2$, namely $J_x^{S_j,(1)} = -\frac{i\hbar}{4m^2c^2}(\vec{\nabla}\phi^\dagger\cdot\vec{\sigma})\widetilde{K}(\vec{r})\sigma_x\sigma_j\phi - \frac{i\hbar}{4m^2c^2}\phi^\dagger\sigma_x\sigma_j\widetilde{K}(\vec{r})(\vec{\sigma}\cdot\vec{\nabla}\phi)$, presents the relativistic effects on spin transport, which is important for the spin Hall and anomalous Hall effects. After some algebra, as derived in Eq. (A9), $J_x^{S_j,(1)}$ contains the term $\frac{\hbar}{4m^2c^2}\phi^\dagger(\vec{\sigma}\times\vec{E})_x\sigma_j\phi$, presenting the spin current transverse to the external field $\vec{E}$ due to the spin Hall effect [49]. It has been demonstrated that the FR spin current operator in Eq. (14) can produce the spin Hall conductivity in linear-response theory agreeing well with experiments and other methods, including both the intrinsic and extrinsic contributions [50–52]. Thus, we believe that Eq. (14) provides the appropriate basis for investigating various important fully relativistic spin transport phenomena, including both current-induced STT and SOT.

To calculate the spin current $J_i^{S_j}$ in Eq. (14) with the first-principles FR-EMTO method, we apply the NEGF technique to rewrite

$$J_i^{S_j}(E,\boldsymbol{r}) = -\frac{ic}{2\pi}\sum_{R\Lambda,R'\Lambda'} G^{<G}_{R'\Lambda',R\Lambda}\Phi^{aG\dagger}_{R\Lambda}(\vec{r})\alpha_i\hat{T}_j\Phi^{aG}_{R'\Lambda'}(\vec{r}).$$

For a disordered device system, containing A_xB_{1-x}, the disorder-averaged spin current density can be given by

$$\overline{J}_i^{S_j} = -\frac{ic}{2\pi}\left[\sum_{R\Lambda\Lambda'}\sum_{Q} C_R^Q\overline{G^{<,Q,G}_{R\Lambda',R\Lambda}}\Phi^{Q,G\dagger}_{R\Lambda}\alpha_i\hat{T}_j\Phi^{Q,G}_{R\Lambda'} + \sum_{R\Lambda R'\Lambda'}^{R\neq R'}\sum_{QQ'} C_R^Q C_{R'}^{Q'}\overline{G^{<,QQ',G}_{R'\Lambda',R\Lambda}}\Phi^{Q,G\dagger}_{R\Lambda}\alpha_i\hat{T}_j\Phi^{Q',G}_{R'\Lambda'}\right], \quad (15)$$

where $\overline{G^{<,Q,G}_{R\Lambda',R\Lambda}}$ and $\overline{G^{<,QQ',G}_{R'\Lambda',R\Lambda}}$ $(Q = A/B)$ are conditionally averaged GFs in the global framework (for more details, please refer to Ref. [25]). The total spin current can be obtained by integration on the surface area, and then the spin torque can be derived. The implementation of the (noncollinear) FR-EMTO-DFT-based spin current formula can provide an important first-principles tool for studying important spin transport phenomena and the associated relativistic effects in the realistic device materials with atomic disorders.

IV. NUMERICAL RESULTS AND DISCUSSIONS

We have implemented the FR noncollinear formalism in Sec. II and the associated spin current formula in Sec. III within the EMTO-DFT-NEGF-based first-principles quantum transport simulation package SIGMAX [24,25,28] using the spherical cell approximation proposed by Vitos [40,53]. Such an FR implementation enables the simulation of electron and spin transport in noncollinear magnetic multilayers and various relativistic transport phenomena (e.g., spin Hall effect) with the influence of disorders and external bias. As an important test for the present FR implementation of the noncollinear EMTO-DFT-NEGF method and spin current in Eq. (14), we calculate the spin current to derive the spin-transfer torque in noncollinear Co/Cu/FM/Cu (FCC 111) spin valves and the important spin-Hall angle in the various disordered alloys Pt_xY_{1-x} (Y = vacancy, Au, Pd, Ag) and compare with previous calculations and experiments. In all our calculations, the local spin density approximation of VWN form [54] is employed for the exchange-correlation functional. The spin current density is calculated on a uniform real-space mesh on a surface to integrate to obtain the total spin current.

A. Spin transfer in noncollinear Co/Cu/FM/Cu spin valves

For the simulation of the spin angular momentum transfer, namely STT, in ferromagnetic (FM) multilayers, the first-principles approaches have been developed to address the specific material dependence, including the calculation of STT by the NEGF-DFT with LCAO basis in Ref. [55], and the scattering-state approach with the TB-LMTO method in the scalar relativistic framework in Refs. [17,56] (in which the effects of disorder on spin transfer are treated with the computationally demanding supercell method). In this section, we present the results of the FR calculation of the STT in noncollinear FM multilayers with nonequilibrium mean-field theory to effectively handle atomic disorders, and we compare them with the results from Ref. [17]. We investigate the spin-polarized transport in different Co/(10ML)Cu/(15ML)FM/Cu (FM=Co, $Ni_{0.8}Fe_{0.2}$) noncollinear spin valves as shown in Fig. 1. Here, for FM = Co, we consider the likely disordered interdiffused interfaces Cu/Co or Co/Cu associated with the central Cu region, namely Cu_xCo_{1-x} alloy, in a single atomic layer. We consider all spin-valve structures in FCC with the lattice constant $a = 3.54$ Å and electron transport along (111) as the $\vec{e}_z$ direction with periodicity in the x-y plane. To ensure the convergence in 2D BZ integration, we use 50×50 $k_\parallel$-mesh for electronic structure self-consistency and 200×200 $k_\parallel$-mesh for spin current calculations, and all the transport results are calculated at E_f.

Figure 2 presents the conductance versus magnetization angle θ between Co and FM for the different disordered

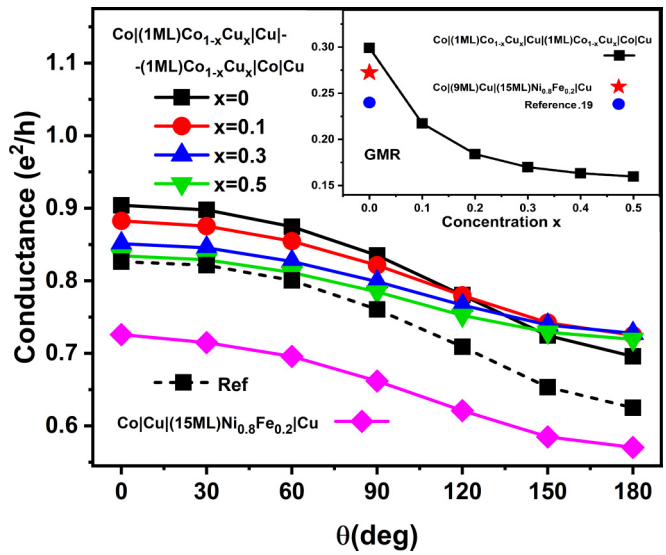

FIG. 2. The conductance vs the noncollinear magnetization angle θ for different Co/Cu/FM/Cu spin valves. Inset: GMR vs disorder concentration x for different spin valves.

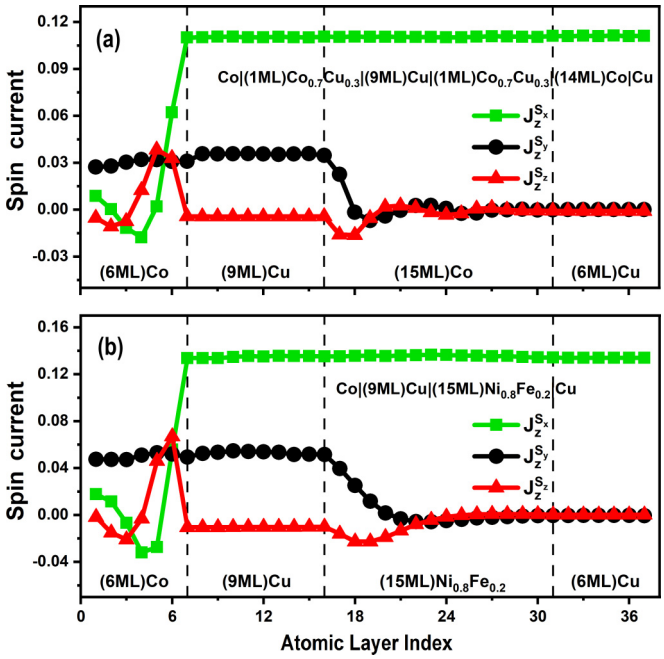

FIG. 3. Spin current vs surface index z for different spin valves with FM = Co and $x = 0.3$ in (a) and FM = $Ni_{0.8}Fe_{0.2}$ alloy in (b).

spin valves with FM = Co and $Ni_{0.8}Fe_{0.2}$. The monotonic decrease in conductance with increasing θ is consistent with the previous *ab initio* results [17,55]. It is found that, for Co/Cu/Co/Cu with $x = 0$, namely with perfect interface, the FR-EMTO results are almost constantly shifted by about 10% over the results of TB-LMTO in Ref. [17] (in the dashed line), and such a difference in conductance can be attributed to the differences between EMTO and TB-LMTO methods (not to the SOI, which is negligible in Cu and Co). By increasing disorder x from 0 to 0.5, the conductance for spin valves with FM = Co can be notably reduced for small θ, while the conductance at $\theta = 180^\circ$ is slightly modulated. The spin valve with FM = $Ni_{0.8}Fe_{0.2}$ presents a similar θ dependence of conductance with magnitude lower than the results of FM = Co. The inset of Fig. 2 shows the GMR, namely GMR = $\frac{G(0^\circ)-G(180^\circ)}{G(180^\circ)}$, versus interface disorder x. At $x = 0$, namely the perfect FM = Co spin valve, our calculated GMR = 29.9%, consistent with the value 24.0% from Ref. [17]. However, as the disorder increases to $x = 0.5$, the GMR is quickly reduced to 16.0%, highlighting the important influence of interface disorder. The GMR value for the spin valve with NiFe alloy is 27.2%, which is close to the value for the perfect valve with FM = Co.

Figure 3 shows the layer-resolved spin current for the spin valves with FM = Co with $x = 0.3$ in (a) and $Fe_{0.2}Ni_{0.8}$ in (b) for $\theta = 90^\circ$. It is clear that, for each spin component, both devices present quite similar layer dependence in spin current. For the studied noncollinear spin valves with almost neglectable SOI, the spin currents present important changes in the central scattering region, namely changing from $J_z^{S_y}$ in the left Co electrode to $J_z^{S_x}$ in the right Cu electrode. In particular, $J_z^{S_x}$ presents a sharp and large enhancement around the left Co/Cu interface from the minimum −0.017 to 0.110 in (a) and −0.032 to 0.134 in (b) (due to the effects of spin reflection at the right Cu/FM interface), and then maintains a constant for $z > 7$. $J_z^{S_y}$ stays almost constant for $z < 17$, and then presents an important decrease for $z > 17$ and becomes zero after $z > 30$. Moreover, $J_z^{S_z}$ presents remarkable magnitude around both Co/Cu and Cu/FM interfaces due to the physical effects of the sudden magnetization change induced effective field, and then quickly changes to zero away from the interfaces [57]. Here, it should be mentioned that the spin current in Eq. (14) with the Bargmann-Wigner spin polarization operator can present the physical results for $J_z^{S_z}$, while the spin current operator $c\alpha_z\beta\Sigma_z$ does not. It is clear that all the spin current $J_z^{S_i}$ $(i = x, y, z)$ for both spin valves is conserved inside the Cu layers. As an important observation, all the spin current components are very sensitive to the interface scattering, presenting the important influences of interfaces on spin transfer. The apparent changes in spin current reflect the important spin transfer torque exerted on the related atomic layers.

Figure 4 shows the spin transfer torque exerted on each atomic layer, which is calculated by the difference in spin currents of neighboring surfaces shown in Fig. 3, namely $\tau_{i,n} = J_{z,n}^{S_i} - J_{z,n+1}^{S_i}$ $(i = x, y, z)$. In our result, τ_x and τ_y correspond to the in-plane torques and τ_z is the out-of-plane torque. It is clear that for both spin valves, the significant in-plane and out-of-plane torques are present in the Co layers at the Co/Cu interface, and both τ_x and τ_z show strong oscillations and quickly decay in a few layers of Co, while τ_y remains almost zero. The large negative and positive values of τ_x and τ_z illustrate the strong omission and absorption of spin angular momentum on the Co atomic layers near the interface. Furthermore, inside the central FM region, while τ_x remains zero, both τ_y and τ_z show an important decay to zero before reaching the Cu electrode. In FM = $Ni_{0.8}Fe_{0.2}$, the spin torques decays to zero within six MLs, while in FM = Co, the spin torques decay to zero within 11 MLs with clear oscillation, which is consistent with the results of Ref. [17]. The different decaying length of spin torque in Co and $Ni_{0.8}Fe_{0.2}$ reflects the different spin decoherence length. Figure 4(b) also includes the results of Ref. [17] in the empty for comparison. It is clear that for the spin valve with $Ni_{0.8}Fe_{0.2}$, the fully relativistic nonequilibrium mean-field calculations of STT agree well with the TB-LMTO scattering state supercell calculation, presenting a good test for the implementation of noncollinear FR-EMTO and the fully relativistic spin current formula. The small difference in magnitude between the present results and those of Ref. [17] can be attributed to the different methods, namely EMTO and TB-LMTO. In Fig. 4(c), we present the total in-plane torque τ_y of the FM region versus the magnetization angle θ for spin valves of FM = Co with different x and FM = $Ni_{0.8}Fe_{0.2}$ (where τ_x and τ_z are negligible). It is found that the total τ_y reaches the maximum around $\theta = 90$, and the results of $Ni_{0.8}Fe_{0.2}$ are higher than that of FM = Co. For valves with FM = Co, at $60 < \theta < 120$, it is found that interface disorder can quickly decrease the result by small x (<10%) and the reduction in torque is rather limited upon further increasing x over 10%. For example, τ_y can be reduced by 25% from the value of 0.004 at $x = 0$–0.003 at $x = 10\%$, presenting the important influence of interfacial disorders. It

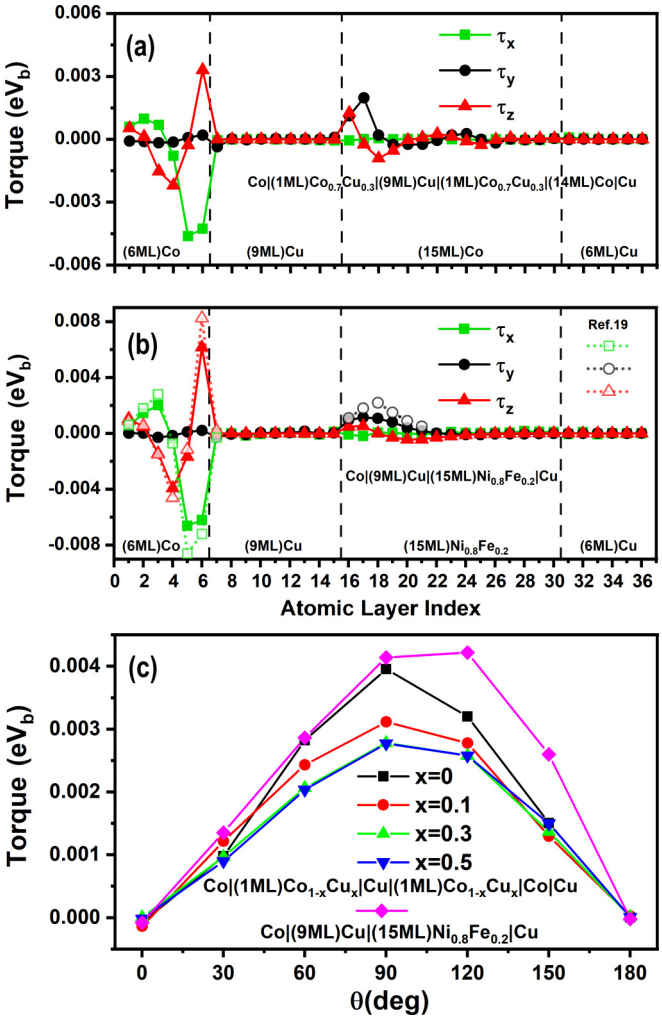

FIG. 4. (a), (b) Spin transfer torque $\tau_{x/y/z}$ vs atomic layer index in spin valves: (a) for FM = Co and $x = 0.3$; (b) for FM = $Ni_{0.8}Fe_{0.2}$ alloy. (c) Spin torque τ_y vs disorder, (b) in-plane torque τ_y vs noncollinear magnetization angle θ for the sandwiched FM layers (FM = Co and $Ni_{0.8}Fe_{0.2}$).

is also clear that the maximum torque of the NiFe alloy (in pink) does not occur at 90° as shown in Fig. 4(c); we attribute the physics to the anisotropy induced by the spin-orbital interaction in FeNi alloy.

B. Spin Hall effect in $Pt_{1-x}Y_x$ alloys: Y = Va, Au, Pd, Ag

It is known that SOI can generate a pure spin current transverse to the electron charge current, known as the spin Hall effect (SHE). In this section, we apply the FR-EMTO-DFT-NEGF first-principles quantum transport method and the FR spin current formula in Eqs. (14) and (15) to calculate the spin current induced by SHE in nonmagnetic $Pt_{1-x}Y_x$ alloys in two-probe device structures. The schematic of the device geometry is shown in Fig. 5, in which the central alloy region is sandwiched by pure Pt electrodes, and the device is periodic in the x-y plane. We simulate all devices in the FCC structure, neglecting the lattice distortion, and we calculate the spin current flowing in the x (FCC 111) direction with the charge flowing in the z (FCC $11\bar{2}$) direction. To ensure the convergence

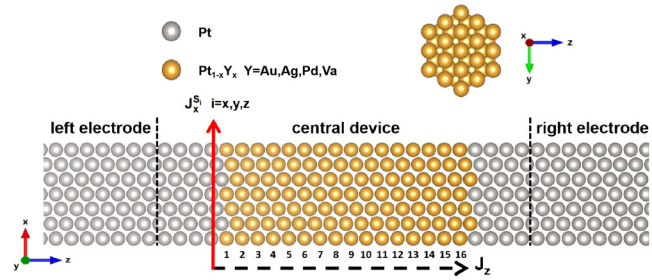

FIG. 5. Schematic illustration for the two-probe simulation of spin Hall effects in the $Pt_{1-x}Y_x$ alloys [Y = vacancy (Va), Pd, Au, and Ag] in FCC. The device is periodic in the x-y plane. The electron charge flows in z, and the spin current flows in x [in the FCC (111) direction]. The inset gives the top view of the device structure.

for the 2D BZ integration, we use 40×100 $k_\parallel$-mesh electronic structure self-consistency and 120×300 $k_\parallel$-mesh for all transport calculations. The spin current is calculated on the surface lying in the middle of two neighboring atomic layers in the (111) direction. The spin Hall angle (SHA), defined as the ratio of transverse spin current to longitudinal charge current, characterizes the conversion efficiency of the charge current to pure spin current.

First, we calculate the layer-resolved spin current $J_x^{S_y}$ for pure Pt and $Pt_{1-x}Va_x$ (with $x = 3\%$ and 6% for disordered vacancies as the intrinsic defects in Pt) in the central device region (the spin currents $J_x^{S_x}$ and $J_x^{S_z}$ are negligible). Figure 6 shows the layer-resolved SHA results $J_x^{S_y}/J_z$ for the system under bias voltages $V_b = 0$ (in solid lines) and $V_b = 0.2V$ (in dotted lines). For $V_b = 0$, the results are calculated at $E = E_f$. For the case $V_b = 0.2V$, the bias is approximately treated by introducing a linear potential in the central yellow region in Fig. 5, and the charge and spin current are calculated by integration with 10 energy points sampled between the chemical potential μ_L and μ_R ($\mu_L - \mu_R = 0.2$ eV). As shown

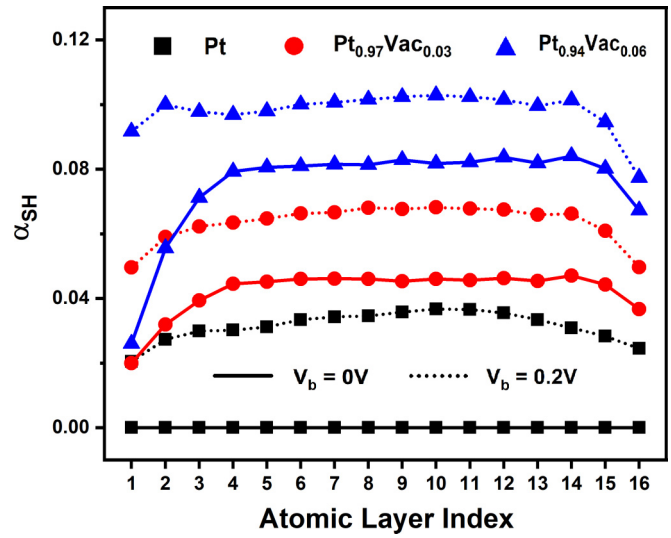

FIG. 6. Spin Hall angle ($\alpha_{SH} = J_x^{S_y}/J_z$) vs atomic layer index of the central device region in yellow with $Pt_{1-x}Va_x$ ($x = 0.0$, 0.03, 0.06).

in Fig. 6, for $V_b = 0$, pure Pt exhibits zero SHA values for all atomic layers, namely no spin current is generated at the energy E_f [namely $J_x^{S_y}(E_f)$] despite the finite conductance, due to the lack of scattering to the propagating wave. To introduce the scattering, a bias voltage is applied to induce a potential gradient in the central device region. When applying $V_b = 0.2$, a finite transverse spin current $J_x^{S_y}$ arises due to the potential gradient scattering. The SHA in pure Pt starts from 2.1% at the first layer, reaches the maximum value of 3.7% at the 10th layer, and then decreases to 2.5% at the right end, indicating the important effect of applied bias on SHE. The finite spin current in pure Pt under finite bias can be attributed to the intrinsic SHE [58,59]. In addition to intrinsic SHE, asymmetry in scattering for up and down spins in the presence of disorders/imperfections gives rise to the extrinsic SHE [51]. By introducing the disordered vacancies in Pt, at $V_b = 0$, both $Pt_{0.97}Va_{0.03}$ and $Pt_{0.94}Va_{0.06}$ present a remarkable SHA due to the presence of disorder scattering, in contrast to the pure Pt. For both systems, the SHA shows a fast increase in the first few layers (index $\leqslant 4$) and then maintains an almost constant plateau in the layers ranging from 4 to 15, and it exhibits a small decrease at the right end. It is clear that SHA is promoted by increasing the concentration of vacancies. In particular, for the middle 10th layer, $Pt_{0.94}Va_{0.06}$ exhibits a SHA value 8.2%, compared to the SHA value of 4.6% in $Pt_{0.97}Va_{0.03}$, indicating the important influence of disorder scattering on SHE in Pt. By applying a bias voltage $V_b = 0.2V$, the SHA (in dotted lines) for all layers in both $Pt_{0.94}Va_{0.06}$ and $Pt_{0.97}Va_{0.03}$ can be significantly increased compared to the values for $V_b = 0$. At the 10th layer, the SHA is promoted by 2.1% in $Pt_{0.94}Va_{0.06}$ and 2.2% in $Pt_{0.97}Va_{0.03}$, indicating the important influence of external bias on SHE. These calculations demonstrate that both disorder scattering and applied external electric fields can make significant contributions to the spin current generated by SHE, and therefore the present fully relativistic quantum transport method provides an important tool for simulating SHE in a realistic device structure at nonequilibrium conditions, beyond linear response.

As a further investigation of the influence of disorder on SHE, we present in Fig. 7 the longitudinal electron conductance (a), transverse spin current (b), and SHA (c) versus the disorder concentration x for three $Pt_{1-x}Y_x$ (Y = Au, Pd, Ag) alloys (all results are calculated at E_f with $V_b = 0$ for the 10th layer). As shown in Fig. 7(a), the conductance of PtPd alloy is significantly higher than that of the other alloys. For example, at $x = 0.45$, the conductance values are 3.69, 1.39, and 0.86 (e^2/h) for the respective PtPd, PtAu, and PtAg alloys. As x increases from 0.05 to 0.45, the conductance significantly decreases in magnitude by 5 times in PtAg and 3.6 times in PtAu, while the decrease in PtPd is much more moderate. It is thus clear that different PtY alloys present distinct scattering strengths of disorders. However, as shown in Fig. 7(b), the dependencies of spin current on x are different for different alloys. In particular, as x changes from 0.05 to 0.45, the spin current presents a monotonic increase in PtPd alloy, an increase followed by saturation in PtAu, while in PtAg alloy, the spin current is significantly enhanced at small x ($x \leqslant 15\%$) and followed by a decrease. The decrease of

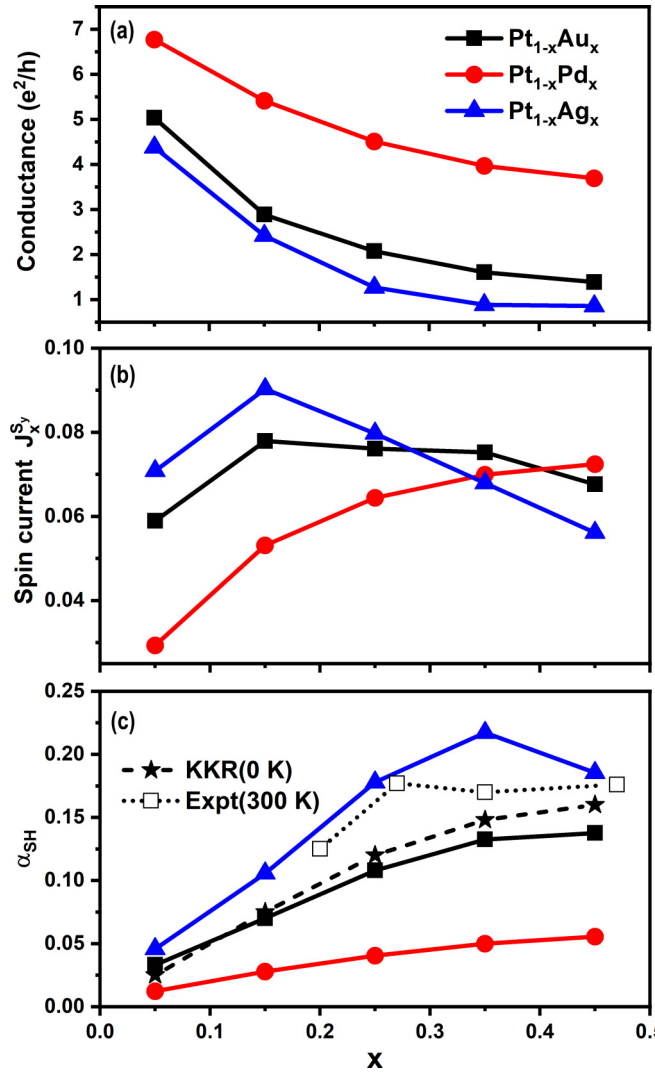

FIG. 7. Conductance, spin Hall current $J_x^{S_y}(E_f)$, and spin Hall angle α_{SH} vs alloy concentration x for $Pt_{1-x}Y_x$ (Y = Au, Ag, Pd).

spin current for increasing $x \geqslant 15\%$ in PtAg can be attributed to the quick decrease in electron conductance, as shown in Fig. 7(a). It is found that spin currents in PtAg and PtAu alloys are significantly higher than that of PtPd alloy for $x \leqslant 15\%$, in contrast to the conductance results in which PtPd conductance is significantly higher than the others. Due to the distinct behavior in the conductance and spin current, for the whole range of disorder x calculated, the $Pt_{1-x}Ag_x$ alloy shows the largest SHA, significantly higher than the others, as shown in Fig. 7(c). Moreover, the SHA of $Pt_{1-x}Pd_x$ is much smaller than the result of PtAu alloy. For example, at $x = 35\%$, the SHA value in PtAg is as large as 21.7%, significantly higher than the value 13.2% in PtAu and 5.0% in PtPd. Thus, we can see that alloying with different elements can provide an effective way to tune the SHE in Pt. Figure 7(c) also includes the experimental SHA for PtAu alloy measured at room temperature (in empty squares) and the results of the first-principles FR-KKR method (in stars) from Ref. [60] for comparison. Our SHA results for PtAu alloy agree well with the FR-KKR calculations, providing an important test for the present implementations. It is clear that the first-principles

results for SHA in PtAu alloy are consistent with the experimental measurements. The deviation between theoretical and experimental results is limited and can be attributed to the fact that the influence of room temperature, which distorts the lattice to increase the scattering and thus SHA, is neglected in the present calculations.

V. CONCLUSIONS

As a summary, we have presented the noncollinear FR-EMTO-DFT-NEGF-based first-principles approach for quantum transport simulation of noncollinear spin transfer and spin Hall current in real device structures with atomic disorders. The Bargmann-Wigner polarization operator is utilized to define the appropriate spin current in FR, so that various spin transport phenomena, such as spin angular momentum transfer in the noncollinear magnetic device and that due to the spin Hall effect, can be studied from first principles. In this approach, the nonequilibrium mean-field method is combined to handle the multiple disorder scattering in both the electronic structure and transport calculations of disordered device materials. We presented applications of this approach to the STT in noncollinear spin valves Co/Cu/FM/Cu (FM = Co, $Ni_{0.8}Fe_{0.2}$) and the spin-Hall angle in various $Pt_{1-x}Y_x$ (Y = vacancy, Au, Ag, Pd) alloys, and our results show good consistency with other previous theoretical calculations and experimental measurements, providing an important test for the implementation of the FR noncollinear formalism and the FR spin current formula. Moreover, we also find that the applied finite bias can significantly enhance the spin Hall angle in $Pt_{1-x}Va_x$ (for $x = 0.0, 0.03, 0.06$), and PtAg alloy presents a much higher spin Hall angle than that of PtAu and PtPd alloys. This work presents an important extension for quantum transport simulation of spintronic materials and devices from first principles.

ACKNOWLEDGMENTS

Y.K. acknowledges financial support from NSFC (Grants No.12227901 and No. 11874265). Z.Y. acknowledges financial support from NSFC (Grant No. 12174028). The authors thank HPC platform of ShanghaiTech University for providing computational facility.

APPENDIX: SPIN CURRENT IN THE NONRELATIVISTIC LIMIT

To investigate the spin current density in the nonrelativistic limit, we start from the Dirac equation $\hat{H}\Psi = E\Psi$ with $\Psi = \binom{\phi}{\chi}$ and H in Eq. (1), namely

$$(E - V(\vec{r}) - \vec{\sigma}\cdot\vec{B}(\vec{r}))\phi - c\vec{\sigma}\cdot\vec{p}\chi = 0,$$
$$-c\vec{\sigma}\cdot\vec{p}\phi + (E - V(\vec{r}) + \vec{\sigma}\cdot\vec{B}(\vec{r}) + 2mc^2)\chi = 0.$$

We can solve to obtain (in the first-order approximation)

$$\begin{aligned}\chi &= \frac{c\vec{\sigma}\cdot\vec{p}}{\widetilde{K}(\vec{r}) + 2mc^2}\phi \\ &= \frac{1}{2mc}\frac{1}{1+\frac{\widetilde{K}(\vec{r})}{2mc^2}}\vec{\sigma}\cdot\vec{p}\phi \\ &\approx \frac{1}{2mc}\left(1 - \frac{\widetilde{K}(\vec{r})}{2mc^2}\right)\vec{\sigma}\cdot\vec{p}\phi \\ &= -\frac{i\hbar\vec{\sigma}}{2mc}\cdot\vec{\nabla}\phi + \frac{\widetilde{K}(\vec{r})}{4m^2c^3}i\hbar\vec{\sigma}\cdot\vec{\nabla}\phi, \end{aligned} \tag{A1}$$

where $\widetilde{K}(\vec{r}) = E - V(\vec{r}) - \vec{\sigma}\cdot\vec{B}(\vec{r})$.

Here, we consider the spin current component $J_x^{s_j}$ in Eq. (14), namely

$$J_x^{S_j} = c\Psi^\dagger\left(\alpha_x\beta\Sigma_j + \frac{\Sigma_x\hat{p}_j}{mc}\right)\Psi, \tag{A2}$$

where

$$\alpha_x\beta\Sigma_j + \frac{\Sigma_x\hat{p}_j}{mc} = \begin{pmatrix} \frac{\sigma_x\hat{p}_j}{mc} & -\sigma_x\sigma_j \\ \sigma_x\sigma_j & \frac{\sigma_x\hat{p}_j}{mc}\end{pmatrix}. \tag{A3}$$

Then, one obtains

$$\begin{aligned} J_x^{S_j} = &\frac{1}{m}\phi^\dagger\sigma_x p_j\phi + c\chi^\dagger\sigma_x\sigma_j\phi \\ &- c\phi^\dagger\sigma_x\sigma_j\chi + \frac{1}{m}\chi^\dagger\sigma_x p_j\chi. \end{aligned} \tag{A4}$$

With the relation in Eq. (A1) for χ, we can obtain the spin current in the nonrelativistic limit with the terms up to the first order of $1/c^2$ as follows:

$$\begin{aligned} J_x^{S_j} = &\frac{-i\hbar}{m}\phi^\dagger\sigma_x\nabla_j\phi \\ &+ \frac{i\hbar}{2m}(\vec{\nabla}\phi^\dagger\cdot\vec{\sigma})\sigma_x\sigma_j\phi \\ &+ \frac{i\hbar}{2m}\phi^\dagger\sigma_x\sigma_j(\vec{\sigma}\cdot\vec{\nabla}\phi) \\ &- \frac{i\hbar}{4m^2c^2}(\vec{\nabla}\phi^\dagger\cdot\vec{\sigma})\widetilde{K}(\vec{r})\sigma_x\sigma_j\phi \\ &- \frac{i\hbar}{4m^2c^2}\phi^\dagger\sigma_x\sigma_j\widetilde{K}(\vec{r})(\vec{\sigma}\cdot\vec{\nabla}\phi), \end{aligned} \tag{A5}$$

where we neglect the first-order term $-\frac{i\hbar^3}{4m^3c^2}(\vec{\nabla}\phi^\dagger\cdot\vec{\sigma})\sigma_x\nabla_j(\vec{\sigma}\cdot\vec{\nabla}\phi)$ obtained from $\frac{1}{m}\chi^\dagger\sigma_x p_j\chi$ due to the very small prefactor.

We first consider the terms with zeroth order of $\frac{1}{c^2}$, namely $J_x^{S_j,(0)}$,

$$\begin{aligned} J_x^{S_j,(0)} = &\frac{-i\hbar}{m}\phi^\dagger\sigma_x\nabla_j\phi + \frac{i\hbar}{2m}(\vec{\nabla}\phi^\dagger\cdot\vec{\sigma})\sigma_x\sigma_j\phi \\ &+ \frac{i\hbar}{2m}\phi^\dagger\sigma_x\sigma_j(\vec{\sigma}\cdot\vec{\nabla}\phi). \end{aligned} \tag{A6}$$

In the following, we investigate $J_x^{S_j,(0)}$ for different $j = x, y, z$:

$$\begin{aligned}
J_x^{S_x,(0)} &= \frac{-i\hbar}{m}\phi^\dagger\sigma_x\nabla_x\phi + \frac{i\hbar}{2m}(\vec{\nabla}\phi^\dagger\cdot\vec{\sigma})\sigma_x\sigma_x\phi + \frac{i\hbar}{2m}\phi^\dagger\sigma_x\sigma_x(\vec{\sigma}\cdot\vec{\nabla})\phi \\
&= \frac{-i\hbar}{m}\phi^\dagger\sigma_x\nabla_x\phi + \frac{i\hbar}{2m}(\nabla_x\phi^\dagger\sigma_x + \nabla_y\phi^\dagger\sigma_y + \nabla_z\phi^\dagger\sigma_z)\sigma_x\sigma_x\phi + \frac{i\hbar}{2m}\phi^\dagger\sigma_x\sigma_x(\sigma_x\nabla_x\phi + \sigma_y\nabla_y\phi + \sigma_z\nabla_z\phi) \\
&= \frac{-i\hbar}{m}\phi^\dagger\sigma_x\nabla_x\phi + \frac{i\hbar}{2m}(\nabla_x\phi^\dagger - i\nabla_y\phi^\dagger\sigma_z + i\nabla_z\phi^\dagger\sigma_y)\sigma_x\phi + \frac{i\hbar}{2m}\phi^\dagger\sigma_x(\nabla_x\phi + i\sigma_z\nabla_y\phi - i\sigma_y\nabla_z\phi) \\
&= \frac{-i\hbar}{m}\phi^\dagger\sigma_x\nabla_x\phi + \frac{i\hbar}{2m}\nabla_x\phi^\dagger\sigma_x\phi + \frac{\hbar}{2m}(\nabla_y\phi^\dagger\sigma_z - \nabla_z\phi^\dagger\sigma_y)\sigma_x\phi + \frac{i\hbar}{2m}\phi^\dagger\sigma_x\nabla_x\phi + \frac{\hbar}{2m}\phi^\dagger\sigma_x(\sigma_y\nabla_z\phi - \sigma_z\nabla_y\phi) \\
&= \frac{i\hbar}{2m}\nabla_x\phi^\dagger\sigma_x\phi - \frac{i\hbar}{2m}\phi^\dagger\sigma_x\nabla_x\phi + \frac{\hbar}{2m}(\nabla_y\phi^\dagger\sigma_z - \nabla_z\phi^\dagger\sigma_y)\sigma_x\phi + \frac{\hbar}{2m}\phi^\dagger\sigma_x(\sigma_y\nabla_z\phi - \sigma_z\nabla_y\phi) \\
&= \frac{i\hbar}{2m}\phi^\dagger[\sigma_x(\overleftarrow{\nabla}_x - \overrightarrow{\nabla}_x)]\phi - \frac{\hbar}{2m}(\nabla_y\phi^\dagger\sigma_z - \nabla_z\phi^\dagger\sigma_y)\sigma_x\phi - \frac{\hbar}{2m}\phi^\dagger\sigma_x(\sigma_y\nabla_z\phi - \sigma_z\nabla_y\phi) \\
&= \frac{i\hbar}{2m}\phi^\dagger[\sigma_x(\overleftarrow{\nabla}_x - \overrightarrow{\nabla}_x)]\phi - \frac{\hbar}{2m}(\vec{\nabla}\phi^\dagger\times\vec{\sigma})_x\sigma_x\phi - \frac{\hbar}{2m}\phi^\dagger\sigma_x(\vec{\sigma}\times\vec{\nabla}\phi)_x \\
&= \frac{i\hbar}{2m}\phi^\dagger[\sigma_x(\overleftarrow{\nabla}_x - \overrightarrow{\nabla}_x)]\phi + \frac{\hbar}{2m}\phi^\dagger\{\sigma_x[(\overleftarrow{\nabla} + \overrightarrow{\nabla})\times\vec{\sigma}]_x\}\phi,
\end{aligned}$$

where the sign change is made due to the fact that $J_x^{S_x}$ is real and the relation that $\mathrm{Re}\{(\nabla_y\phi^\dagger\sigma_z - \nabla_z\phi^\dagger\sigma_y)\sigma_x\phi + \phi^\dagger\sigma_x(\sigma_y\nabla_z\phi - \sigma_z\nabla_y\phi)\} = 0$, which can be found by using $(\nabla_y\phi^\dagger\sigma_y\phi + \phi^\dagger\sigma_y\nabla_y\phi)^\dagger = (\nabla_y\phi^\dagger\sigma_y\phi + \phi^\dagger\sigma_y\nabla_y\phi)$ and $(\nabla_z\phi^\dagger\sigma_z\phi + \phi^\dagger\sigma_z\nabla_z\phi)^\dagger = (\nabla_z\phi^\dagger\sigma_z\phi + \phi^\dagger\sigma_z\nabla_z\phi)$. Similarly, we can find $J_x^{S_y,(0)}$ and $J_x^{S_z,(0)}$ to finally obtain

$$\begin{aligned}
J_x^{S_j,(0)} = &\frac{i\hbar}{2m}\phi^\dagger[\sigma_j(\overleftarrow{\nabla}_x - \overrightarrow{\nabla}_x)]\phi \\
&+ \frac{\hbar}{2m}\phi^\dagger\{\sigma_j[(\overleftarrow{\nabla} + \overrightarrow{\nabla})\times\vec{\sigma}]_x\}\phi, \qquad \text{(A7)}
\end{aligned}$$

in which the first term is the conventional spin current, and the second term is due to the moving-dipole-induced bound current.

We now consider the terms in first order of $\frac{1}{c^2}$, namely

$$\begin{aligned}
J_x^{S_j,(1)} = &-\frac{i\hbar}{4m^2c^2}(\vec{\nabla}\phi^\dagger\cdot\vec{\sigma})\widetilde{K}(\vec{r})\sigma_x\sigma_j\phi \\
&- \frac{i\hbar}{4m^2c^2}\phi^\dagger\sigma_x\sigma_j\widetilde{K}(\vec{r})(\vec{\sigma}\cdot\vec{\nabla}\phi) \qquad \text{(A8)}
\end{aligned}$$

in which

$$\begin{aligned}
&-(\vec{\nabla}\phi^\dagger\cdot\vec{\sigma})\widetilde{K}(\vec{r})\sigma_x\sigma_j\phi - \phi^\dagger\sigma_x\sigma_j\widetilde{K}(\vec{r})(\vec{\sigma}\cdot\vec{\nabla}\phi) \\
&= -\vec{\nabla}\cdot(\phi^\dagger\vec{\sigma}\widetilde{K}(\vec{r})\sigma_x\sigma_j\phi) + \phi^\dagger(\vec{\sigma}\cdot\vec{\nabla}\widetilde{K}(\vec{r}))\sigma_x\sigma_j\phi \\
&\quad + \phi^\dagger\widetilde{K}(\vec{r})(\vec{\sigma}\cdot\vec{\nabla})\sigma_x\sigma_j\phi - \phi^\dagger\widetilde{K}(\vec{r})\sigma_x\sigma_j(\vec{\sigma}\cdot\vec{\nabla}\phi).
\end{aligned}$$

Here, we can find that

$$\begin{aligned}
&\phi^\dagger(\vec{\sigma}\cdot\vec{\nabla}\widetilde{K}(\vec{r}))\sigma_x\sigma_j\phi \\
&= -\phi^\dagger(\vec{\sigma}\cdot\vec{E})\sigma_x\sigma_j\phi \\
&= -\phi^\dagger(\sigma_x\widetilde{E}_x + \sigma_y\widetilde{E}_y + \sigma_z E_z)\sigma_x\sigma_j\phi \\
&= -\phi^\dagger(E_x - i\sigma_z E_y + i\sigma_y E_z)\sigma_j\phi \\
&= -\phi^\dagger[E_x\sigma_j + i(\vec{\sigma}\times\vec{E})_x\sigma_j]\phi,
\end{aligned}$$

in which the second term gives rise to the transverse spin current due to applied external electric field (for $j \neq x$), known for the spin Hall effect. As a result, we can write down the spin current up to first order of $\frac{1}{c^2}$,

$$\begin{aligned}
J_x^{S_j,(1)} = &-\frac{i\hbar}{4m^2c^2}\vec{\nabla}\cdot(\phi^\dagger\vec{\sigma}\widetilde{K}(\vec{r})\sigma_x\sigma_j\phi) \\
&+ \frac{i\hbar}{4m^2c^2}\phi^\dagger\widetilde{K}(\vec{r})(\vec{\sigma}\cdot\vec{\nabla})\sigma_x\sigma_j\phi \\
&- \frac{i\hbar}{4m^2c^2}\phi^\dagger\widetilde{K}(\vec{r})\sigma_x\sigma_j(\vec{\sigma}\cdot\vec{\nabla}\phi) \\
&- \frac{i\hbar}{4m^2c^2}\phi^\dagger[E_x\sigma_j + i(\vec{\sigma}\times\vec{E})_x\sigma_j]\phi. \qquad \text{(A9)}
\end{aligned}$$

Divergence of the moving-dipole spin current

For the divergence of the moving-dipole term in the zeroth-order spin current in Eq. (A7), we can obtain

$$\begin{aligned}
&\vec{\nabla}\cdot[(\vec{\nabla}\phi^\dagger\times\vec{\sigma})\sigma_j\phi] - \vec{\nabla}\cdot[\phi^\dagger\sigma_j(\vec{\sigma}\times\vec{\nabla}\phi)] \\
&= \vec{\nabla}\cdot[\sigma_j(\vec{\nabla}\phi^\dagger\times\vec{\sigma})]\phi + [\sigma_j(\vec{\nabla}\phi^\dagger\times\vec{\sigma})]\cdot\vec{\nabla}\phi \\
&\quad -\vec{\nabla}\phi^\dagger\cdot[\sigma_j(\vec{\sigma}\times\vec{\nabla}\phi)] - \phi^\dagger\sigma_j\vec{\nabla}\cdot[(\vec{\sigma}\times\vec{\nabla}\phi)] \\
&= [\sigma_j(\vec{\nabla}\phi^\dagger\times\vec{\sigma})]\cdot\vec{\nabla}\phi - \vec{\nabla}\phi^\dagger\cdot[\sigma_j(\vec{\sigma}\times\vec{\nabla}\phi)] \\
&= 0 \qquad \text{(A10)}
\end{aligned}$$

by using the relations $\vec{\nabla}\cdot[(\vec{\sigma}\times\vec{\nabla}\phi)]=0$ and $\vec{\nabla}\cdot[(\vec{\nabla}\phi^\dagger\times\vec{\sigma})]=0$, and $[\sigma_j(\vec{\nabla}\phi^\dagger\times\vec{\sigma})]\cdot\vec{\nabla}\phi = \vec{\nabla}\phi^\dagger\cdot[\sigma_j(\vec{\sigma}\times\vec{\nabla}\phi)]$. As a result, the moving-dipole term has no contribution to the spin torque.

[1] S. A. Wolf, D. D. Awschalom, R. A. Buhrman, J. M. Daughton, S. von Molnár, M. L. Roukes, A. Y. Chtchelkanova, and D. M. Treger, Spintronics: A spin-based electronics vision for the future, Science **294**, 1488 (2001).

[2] I. Žutić, J. Fabian, and S. Das Sarma, Spintronics: Fundamentals and applications, Rev. Mod. Phys. **76**, 323 (2004).
[3] A. Hirohata and K. Takanashi, Future perspectives for spintronic devices, J. Phys. D **47**, 193001 (2014).
[4] A. Manchon, J. Zelezny, I. M. Miron, T. Jungwirth, J. Sinova, A. Thiaville, K. Garello, and P. Gambardella, Current-induced spin-orbit torques in ferromagnetic and antiferromagnetic systems, Rev. Mod. Phys. **91**, 035004 (2019).
[5] J. C. Slonczewski, Current-driven excitation of magnetic multilayers, J. Magn. Magn. Mater. **159**, L1 (1996).
[6] L. Berger, Emission of spin waves by a magnetic multilayer traversed by a current, Phys. Rev. B **54**, 9353 (1996).
[7] R. Ramaswamy, J. M. Lee, K. Cai, and H. Yang, Emission of spin waves by a magnetic multilayer traversed by a current, Appl. Phys. Rev. **5**, 031107 (2018).
[8] J. Sinova, S. O. Valenzuela, J. Wunderlich, C. H. Back, and T. Jungwirth, Spin Hall effects, Rev. Mod. Phys. **87**, 1213 (2015).
[9] L. Liu, T. Moriyama, D. C. Ralph, and R. A. Buhrman, Spin-Torque Ferromagnetic Resonance Induced by the Spin Hall Effect, Phys. Rev. Lett. **106**, 036601 (2011).
[10] L. Liu, C.-F. Pai, Y. Li, H. W. Tseng, D. C. Ralph, and R. A. Buhrman, Spin-Torque switching with the giant spin Hall effect of tantalum, Science **336**, 555 (2012).
[11] L. Liu, O. J. Lee, T. J. Gudmundsen, D. C. Ralph, and R. A. Buhrman, Current-Induced Switching of Perpendicularly Magnetized Magnetic Layers Using Spin Torque from the Spin Hall Effect, Phys. Rev. Lett. **109**, 096602 (2012).
[12] A. G. Aronov and Y. B. Lyanda-Geller, Nuclear electric resonance and orientation of carrier spins by an electric field, JETP Lett. **50**, 431 (1989).
[13] V. M. Edelstein, Spin polarization of conduction electrons induced by electric current in two-dimensional asymmetric electron systems, Solid State Commun. **73**, 233 (1990).
[14] A. Chernyshov, M. Overby, X. Liu, J. K. Furdyna, Y. Lyanda-Geller, and L. P. Rokhinson, Evidence for reversible control of magnetization in a ferromagnetic material by means of spin-orbit magnetic field, Nat. Phys. **5**, 656 (2009).
[15] I. M. Miron, G. Gaudin, S. Auffret, B. Rodmacq, A. Schuhl, S. Pizzini, J. Vogel, and P. Gambardella, Current-driven spin torque induced by the Rashba effect in a ferromagnetic metal layer, Nat. Mater. **9**, 230 (2010).
[16] I. M. Miron, K. Garello, G. Gaudin, P.-J. Zermatten, M. V. Costache, S. Auffret, S. Bandiera, B. Rodmacq, A. Schuhl, and P. Gambardella, Perpendicular switching of a single ferromagnetic layer induced by in-plane current injection, Nature (London) **476**, 189 (2011).
[17] S. Wang, Y. Xu, and K. Xia, First-principles study of spin-transfer torques in layered systems with noncollinear magnetization, Phys. Rev. B **77**, 184430 (2008).
[18] L. Wang, R. J. H. Wesselink, Y. Liu, Z. Yuan, K. Xia, and P. J. Kelly, Giant Room Temperature Interface Spin Hall and Inverse Spin Hall Effects, Phys. Rev. Lett. **116**, 196602 (2016).
[19] V. P. Amin, J. Zemen, and M. D. Stiles, Interface-Generated Spin Currents, Phys. Rev. Lett. **121**, 136805 (2018).
[20] L.-D. Yuan, Z. Wang, J.-W. Luo, E. I. Rashba, and A. Zunger, Giant momentum-dependent spin splitting in centrosymmetric low-Z antiferromagnets, Phys. Rev. B **102**, 014422 (2020).
[21] J. Železný, Y. Zhang, C. Felser, and B. Yan, Spin-Polarized Current in Noncollinear Antiferromagnets, Phys. Rev. Lett. **119**, 187204 (2017).
[22] A. Fert and P. M. Levy, Spin Hall Effect Induced by Resonant Scattering on Impurities in Metals, Phys. Rev. Lett. **106**, 157208 (2011).
[23] Y. Niimi, Y. Kawanishi, D. H. Wei, C. Deranlot, H. X. Yang, M. Chshiev, T. Valet, A. Fert, and Y. Otani, Giant Spin Hall Effect Induced by Skew Scattering from Bismuth Impurities inside Thin Film CuBi Alloys, Phys. Rev. Lett. **109**, 156602 (2012).
[24] Q. Zhang, J. Yan, Y. Zhang, and Y. Ke, Exact muffin tin orbital based first-principles method for electronic-structure and electron-transport simulation of device materials, Phys. Rev. B **100**, 075134 (2019).
[25] Z. Chen, Q. Zhang, Y. Zhang, L. Wang, M. Sang, and Y. Ke, Exact muffin-tin orbital based fully relativistic simulation of device materials: Electronic charge and spin current, Phys. Rev. B **102**, 035405 (2020).
[26] M. H. Hettler, A. N. Tahvildar-Zadeh, M. Jarrell, T. Pruschke, and H. R. Krishnamurthy, Nonlocal dynamical correlations of strongly interacting electron systems, Phys. Rev. B **58**, R7475(R) (1998).
[27] M. H. Hettler, M. Mukherjee, M. Jarrell, and H. R. Krishnamurthy, Dynamical cluster approximation: Nonlocal dynamics of correlated electron systems, Phys. Rev. B **61**, 12739 (2000).
[28] Y. Zhang, J. Zhai, Z. Chen, Q. Zhang, and Y. Ke, First-principles nonequilibrium dynamical cluster theory for quantum transport simulations of disordered nanoelectronic devices, Phys. Rev. B **104**, 115412 (2021).
[29] Y. Zhang, Q. Zhang, Y. Ke, and K. Xia, Giant influence of clustering and anti-clustering of disordered surface roughness on electronic tunneling, Chin. Phys. Lett. **39**, 087301 (2022).
[30] P. Soven, Coherent-Potential model of substitutional disordered alloys, Phys. Rev. **156**, 809 (1967).
[31] D. W. Taylor, Vibrational properties of imperfect crystals with large defect concentrations, Phys. Rev. **156**, 1017 (1967).
[32] Y. Ke, K. Xia, and H. Guo, Disorder Scattering in Magnetic Tunnel Junctions: Theory of Nonequilibrium Vertex Correction, Phys. Rev. Lett. **100**, 166805 (2008).
[33] J. Yan, S. Wang, K. Xia, and Y. Ke, First-principles quantum transport method for disordered nanoelectronics: Disorder-averaged transmission, shot noise, and device-to-device variability, Phys. Rev. B **95**, 125428 (2017).
[34] J. Yan and Y. Ke, Generalized nonequilibrium vertex correction method in coherent medium theory for quantum transport simulation of disordered nanoelectronics, Phys. Rev. B **94**, 045424 (2016).
[35] V. Kumar, O. K. Andersen, and A. Mookerjee, *Lectures on Methods of Electronic Structure Calculations* (World Scientific, Singapore, 1995).
[36] O. K. Andersen, C. Arcangeli, R. W. Tank, T. Saha-Dasgupta, G. Krier, O. Jepsen, and I. Dasgupta, Third-Generation TB-LMTO, MRS Proc. **491**, 3 (1997).
[37] O. K. Andersen and T. Saha-Dasgupta, Muffin-tin orbitals of arbitrary order, Phys. Rev. B **62**, R16219(R) (2000).
[38] O. K. Andersen, T. Saha-Dasgupta, R. W. Tank, C. Arcangeli, O. Jepsen, and G. Krier, *Electronic Structure and Physical*

Properties of Solids, edited by H. Dreyssé (Springer, Berlin, 2000), pp. 3–84.

[39] L. Vitos, Total-energy method based on the exact muffin-tin orbitals theory, Phys. Rev. B **64**, 014107 (2001).

[40] L. Vitos, *Computational Quantum Mechanics for Materials Engineers: The EMTO Method and Applications* (Springer, London, 2007).

[41] I. Turek, V. Drchal, J. Kudrnovský, M. Šob, and P. Weinberger, *Electronic Structure of Disordered Alloys, Surfaces and Interfaces* (Springer US, Boston, 1997).

[42] V. Bargmann and E. P. Wigner, Group theoretical discussion of relativistic wave equations, Proc. Natl. Acad. Sci. USA **34**, 211 (1948).

[43] H. Ebert, Two ways to perform spin-polarized relativistic linear muffin-tin-orbital calculations, Phys. Rev. B **38**, 9390 (1988).

[44] L. V. Pourovskii, A. V. Ruban, L. Vitos, H. Ebert, B. Johansson, and I. A. Abrikosov, Fully relativistic spin-polarized exact muffin-tin-orbital method, Phys. Rev. B **71**, 094415 (2005).

[45] L. V. Keldysh, Diagram technique for nonequilibrium processes, Sov. Phys.-JETP **20**, 1018 (1965).

[46] R. A. Craig, Perturbation expansion for real-time Green's functions, J. Math. Phys. **9**, 605 (1968).

[47] Q.-F. Sun and X. C. Xie, Definition of the spin current: The angular spin current and its physical consequences, Phys. Rev. B **72**, 245305 (2005).

[48] J. Shi, P. Zhang, D. Xiao, and Q. Niu, Proper Definition of Spin Current in Spin-Orbit Coupled Systems, Phys. Rev. Lett. **96**, 076604 (2006).

[49] A. Vernes, B. L. Györffy, and P. Weinberger, Spin currents, spin-transfer torque, and spin-Hall effects in relativistic quantum mechanics, Phys. Rev. B **76**, 012408 (2007).

[50] S. Lowitzer, D. Ködderitzsch, and H. Ebert, Spin projection and spin current density within relativistic electronic-transport calculations, Phys. Rev. B **82**, 140402(R) (2010).

[51] S. Lowitzer, M. Gradhand, D. Ködderitzsch, D. V. Fedorov, I. Mertig, and H. Ebert, Extrinsic and Intrinsic Contributions to the Spin Hall Effect of Alloys, Phys. Rev. Lett. **106**, 056601 (2011).

[52] D. Ködderitzsch, K. Chadova, and H. Ebert, Linear response Kubo-Bastin formalism with application to the anomalous and spin Hall effects: A first-principles approach, Phys. Rev. B **92**, 184415 (2015).

[53] L. Vitos, H. L. Skriver, B. Johansson, and J. Kollár, Application of the Exact Muffin-Tin Orbitals Theory: The Spherical Cell Approximation, Comput. Mater. Sci. **18**, 24 (2000).

[54] S. H. Vosko, L. Wilk, and M. Nusair, Accurate spin-dependent electron liquid correlation energies for local spin density calculations: a critical analysis, Can. J. Phys. **58**, 1200 (1980).

[55] P. M. Haney, D. Waldron, R. A. Duine, A. S. Núñez, H. Guo, and A. H. MacDonald, Current-induced order parameter dynamics: Microscopic theory applied to Co/Cu/Co spin valves, Phys. Rev. B **76**, 024404 (2007).

[56] Z. Yuan and P. J. Kelly, Spin-orbit-coupling induced torque in ballistic domain walls: Equivalence of charge-pumping and nonequilibrium magnetization formalisms, Phys. Rev. B **93**, 224415 (2016).

[57] J. Xiao, A. Zangwill, and M. D. Stiles, Spin-transfer torque for continuously variable magnetization, Phys. Rev. B **73**, 054428 (2006).

[58] Y. Yao and Z. Fang, Sign Changes of Intrinsic Spin Hall Effect in Semiconductors and Simple Metals: First-Principles Calculations, Phys. Rev. Lett. **95**, 156601 (2005).

[59] G. Y. Guo, Y. Yao, and Q. Niu, *Ab initio* Calculation of the Intrinsic Spin Hall Effect in Semiconductors, Phys. Rev. Lett. **94**, 226601 (2005).

[60] M. Obstbaum, M. Decker, A. K. Greitner, M. Haertinger, T. N. G. Meier, M. Kronseder, K. Chadova, S. Wimmer, D. Ködderitzsch, H. Ebert, and C. H. Back, Tuning Spin Hall Angles by Alloying, Phys. Rev. Lett. **117**, 167204 (2016).